JOURNAL OF THERMOPHYSICS AND HEAT TRANSFER
Vol. 23, No. 3, July–September 2009

Two-Dimensional Analytical Model of Heat Transfer for Flames in Channels

Ananthanarayanan Veeraragavan,* Kiran Dellimore,† and Christopher Cadou‡
University of Maryland, College Park, Maryland 20742

DOI: 10.2514/1.39317

A two-dimensional model for heat transfer in reacting channel flow with a constant wall temperature is developed along with an analytical solution that relates the temperature field in the channel to the flow Péclet number. The solution is derived from first principles by modeling the flame as a volumetric heat source and by applying jump conditions across the flame for plug and Hagen–Poiseuille velocity profiles and is validated via comparison with more detailed computational fluid dynamics solutions. The analytical solution provides a computationally efficient tool for exploring the effects of varying channel height and gas velocity on the temperature distribution in a channel in which a flame is stabilized. The results show that the Péclet number is the principal parameter controlling the temperature distribution in the channel. It is also found that although the Nusselt number is independent of the Péclet number (or velocity) in the postflame region, it can change by nearly 3 orders of magnitude in the preflame region over the range of Péclet numbers (or velocities) expected in microcombustors. This has important implications for quasi-one-dimensional numerical modeling of micro/mesoscale combustion, in which it is usual to select a single Nusselt value from the heat transfer literature. A correlation to facilitate incorporation of the streamwise Nusselt number variation is provided.

Nomenclature

A_n	=	nth coefficient in the preflame solution for the nondimensional temperature variable
B_n	=	nth coefficient in the postflame solution for the nondimensional temperature variable
Cp	=	specific heat capacity of gas
d	=	channel width, m
k	=	thermal conductivity of gas
Nu	=	Nusselt number
Pe	=	Péclet number
Pr	=	Prandtl number
$\dot{q}'''_R$	=	volumetric heat released in the flame
T	=	temperature, K
U	=	flow velocity, m/s
$\bar{U}$	=	average velocity
U^+	=	nondimensional velocity
X	=	function invoked in separation of variables solution for the x^+ variable
x	=	spatial variable along flow direction, m
x^+	=	nondimensional spatial variable along flow direction
Y	=	function invoked in separation of variables solution for the y^+ variable
y	=	spatial variable transverse to flow direction, m
y^+	=	nondimensional spatial variable transverse to flow direction
α_n	=	nth generic eigenvalue
β_n	=	nth postflame eigenvalue
δ	=	Dirac delta function
θ	=	nondimensional temperature
λ_n	=	nth preflame eigenvalue
ρ	=	density, kg/m^3
ϕ	=	preflame eigenfunction
ψ	=	postflame eigenfunction

Presented as Paper 3899 at the 39th AIAA Thermophysics Conference, Miami, FL, 25–28 June 2007; received 30 June 2008; revision received 7 January 2009; accepted for publication 25 January 2009.

*Ph.D. Candidate, Aerospace Engineering, 0134 Engineering Laboratory Building 89.

†Graduate Student, Aerospace Engineering, 0134 Engineering Laboratory Building 89.

‡Associate Professor, Aerospace Engineering, 3179D Glenn L. Martin Hall.

I. Introduction

THE demand for compact propulsion systems for microsatellites and micro unmanned air vehicles, in addition to the demand for compact high-power-density sources in general, has generated considerable interest in millimeter- and submillimeter-scale combustors that are capable of operating on high energy-density hydrocarbon fuels. This has led to a number of efforts to build microscale combustors [1] and to model reacting flows in small passages [2–5]. These investigations have found that the strength of the thermal coupling between the reacting gas and the structure has important, and often dominant, effects on the behavior and stability of flames. Distinguishing effects of combustion in microchannels include increased sensitivity to thermal (and chemical) quenching, increased burning velocity, broadened stability limits, and broadened reaction zones. These findings in microchannels are consistent with earlier experimental and theoretical work in heat recirculating or excess enthalpy burners [6–8]. Asymptotic expansion methods have also been used to develop models for reacting flows in small channels [9,10]. The work presented here considers the microchannel combustion problem from a heat transfer point of view by developing a simple analytical model for the temperature field in the gas that results from spatially localized combustion. The principal aspects of the microcombustion problem considered are operation at low Péclet numbers and the two-dimensional nature of the heat transfer process. Although rarefaction effects can become important at very small length scales (approximately one-hundredth of a flame thickness), heat losses to the environment at such tiny scales renders combustion impractically inefficient. Therefore, this work focuses on larger scales in which the fluid remains in the continuum and it is possible to design devices with practical thermal efficiencies (i.e., greater than 50%).

There is extensive literature describing heat transfer in channel flows [11–15]. It begins with the classical Graetzian problem [11], first solved in the 19th century, which focuses on steady heat transfer between a channel flow and the walls. The basis of the Graetz problem is an energy balance between convective transport in the

axial direction and heat conduction in the transverse direction. A variety of extensions to this solution have been developed over the years for various purposes, but those that are most relevant to the flame problem are those in which axial conduction in the gas is also included [12–15]. Yin and Bau [12] have solved the conjugate heat transfer problem for a flow in a passage in which they mathematically address the heat transfer between the solid and fluid. They highlight the difficulty in solving this problem mathematically, as this problem is not a typical Sturm–Liouville-type equation, owing to the nonlinear appearance of the eigenvalues in the governing equations. In this spirit, the work presented here is a similar extension of the Graetz problem that accounts for the effects of spatially localized heat release associated with a flame stabilized in a channel.

II. Mathematical Model

Figure 1 illustrates the basic physical problem. A flame is stabilized in the infinite channel formed between two parallel plates. Reactants are fed into the channel from the left side at exactly the right velocity (the flame speed) so that the flame position remains fixed in the laboratory reference frame. Hot combustion products in the postflame zone heat the walls of the channel which, in turn, preheat the reactants entering the reaction zone. The governing equation for this problem is conservation of energy in the gas [Eq. (1)], in which the heat release at the flame is modeled using a concentrated volumetric heat release function:

$$\rho U(y) Cp \frac{\partial T}{\partial x} = k_g \left(\frac{\partial^2 T}{\partial x^2} + \frac{\partial^2 T}{\partial y^2} \right) + \dot{q}'''_R \frac{\delta(x)}{1/d} \tag{1}$$

The walls are assumed to be at a uniform temperature, and the temperature of the inlet and outlet streams are assumed to be equal to the wall temperature. The temperature profile in the gas is assumed to be symmetric about the centerline, based on the symmetry of the problem. This leads to the following boundary conditions:

$$T(\mp\infty, y) = T_W \tag{2a}$$

$$\left. \frac{\partial T}{\partial y} \right|_{y=0} = 0 \tag{2b}$$

Equation (1) is rewritten in terms of the following nondimensional variables:

$$\theta = \frac{T - T_W}{\dot{q}'''_R d^2 / k_g}; \qquad x^+ = \frac{x}{d}; \qquad y^+ = \frac{y}{d}$$
$$U^+(y^+) = U(y^+)/\bar{U} \tag{3}$$

where

$$\bar{U} = \int_0^1 U(y^+) \mathrm{d}y^+ = \begin{cases} U; & \{U(y^+) = U \text{ (plug flow)}\} \\ \frac{2}{3} U_{\max}; & \{U(y^+) = U_{\max}(1 - y^{+2}) \text{ (Hagen–Poiseuille flow)}\} \end{cases} \tag{4}$$

This leads to the nondimensional energy equation:

$$PeU^+(y^+) \frac{\partial \theta}{\partial x^+} = \frac{\partial^2 \theta}{\partial x^{+2}} + \frac{\partial^2 \theta}{\partial y^{+2}} + \delta(x^+) \tag{5}$$

where Pe is the Péclet number, a ratio of convective to conductive heat transfer.

$$Pe = Re\, Pr = \frac{\rho \bar{U} Cp d}{k_g} \tag{6}$$

The boundary conditions transform to

$$\theta(\mp\infty, y^+) = 0 \tag{7a}$$

$$\left. \frac{\partial \theta}{\partial y^+} \right|_{y^+=0} = 0 \tag{7b}$$

$$\theta(x^+, 1) = 0 \tag{7c}$$

Equation (7b) arises from considerations of symmetry about the centerline, and Eq. (7c) arises from the constant-wall-temperature assumption. At the flame itself, we require that the temperatures on both sides of the flame are equal:

$$\theta(0^-, y^+) = \theta(0^+, y^+) \tag{8a}$$

Integrating the energy equation over an infinitesimally small volume around the flame as follows,

$$\int_{0^-}^{0^+} \left(PeU^+(y^+) \frac{\partial \theta}{\partial x^+} = \frac{\partial^2 \theta}{\partial x^{+2}} + \frac{\partial^2 \theta}{\partial y^{+2}} + \delta(x^+) \right) \mathrm{d}x^+ \tag{8b}$$

gives the jump condition across the flame sheet:

$$\left. \frac{\partial \theta}{\partial x^+} \right|_{0^-}^{0^+} = -1 \tag{8c}$$

III. Solution

We seek a separation of variables solution for the temperature field in the nondimensional streamwise and spanwise coordinate directions x^+ and y^+, respectively. Thus,

$$\theta(x^+, y^+) = X(x^+) Y(y^+) \tag{9}$$

Substituting Eq. (9) into energy equation (5) leads to

$$\frac{-(X'' - PeU^+(y^+)X')}{X} = \frac{Y''}{Y} \tag{10}$$

We seek solutions for the X functions that satisfy Eq. (11):

$$\frac{X'}{X} = \pm\alpha \tag{11}$$

The choice of the plus or minus comes from whether we are interested in the preflame or postflame solutions. Although Eq. (11) seems reasonable because it meets the boundary conditions at $x \to \pm\infty$ and similar approaches have been taken elsewhere [12,13], computational fluid dynamics (CFD) simulations will be used later in the paper to demonstrate that solutions of this form give accurate results for fully developed Hagen–Poiseuille (H-P) flow. Substituting Eq. (11) in Eq. (10) gives the following ordinary differential equation (ODE) for Y:

$$Y'' + (\alpha^2 \mp \alpha Pe\, U^+(y^+)) Y = 0 \tag{12}$$

With boundary conditions [arising from Eqs. (7b) and (7c)]

$$Y'(0) = 0 \tag{13a}$$

$$Y(1) = 0 \tag{13b}$$

When the velocity profile is flat [as in plug flow, where $U^+(y^+) = 1$], Eq. (12) is a wave equation with the following solution:

$$Y(y^+) = (C_n \cos(\alpha_n, y^+) + D_n \sin(\alpha_n, y^+)) \tag{14}$$

When the velocity profile is parabolic [as in H-P- flow, where $U^+(y^+) = 3/2(1 - y^{+2})$], Eq. (12) can be solved after a transformation of variables to give the following solution:

$$Y(y^+) = (C_n \text{ Hypergeometric1}F1(a1, b1, c1) + D_n \text{ HermiteH } (a2, b2))e^{PIy^{+2}} \quad (15)$$

Definitions of the parameters in Eq. (15) are provided in Table 1. The solutions to Eq. (12) can be written more generically as

$$Y(y^+) = (C_n Y_1(\alpha_n, y^+) + D_n Y_2(\alpha_n, y^+)) \quad (16)$$

where Y_1 is a placeholder for either the cosine or the Hypergeometric1F1 function (depending on the choice of the velocity profile), and Y_2 is a placeholder for the sine or the HermiteH function. In each case, one of the functions (the HermiteH or sine) does not satisfy the boundary condition at the centerline and therefore is not admissible as a solution. For example, substituting Eq. (16) in Eq. (13a) gives

$$Y'(0) = (C_n Y_1'(\alpha_n, y^+) + D_n Y_2'(\alpha_n, y^+)) = 0 \quad (17)$$

This leads to

$$D_n Y_2'(\alpha_n, 0) = 0 \quad \text{or} \quad D_n = 0 \quad (18)$$

because

$$Y_1'(\alpha_n, 0) = 0 \quad \text{and} \quad Y_2'(\alpha_n, 0) \neq 0 \quad (19)$$

Because Y_2 does not satisfy the boundary condition at the centerline, Y_1 is left as the only solution to the ODE. Demanding that the Y_1 function satisfy Eq. (13b) (the other boundary condition at the wall) allows us to obtain the eigenvalues α_n: that is,

$$Y_1(\alpha_n, 1) = 0 \quad (20)$$

Obtaining the eigenvalues α_n in the case of plug flow is easier, as the roots of the cosine function are well known. However, in the case of Hagen–Poiseuille flow, the eigenvalues α_n have to be determined numerically, because the roots of the Hypergeometric1F1 function do not have a closed form. Also note that because the ODE is different in the pre- and postflame regions (because of the minus or plus sign), the resulting solutions to the ODE are different in the two regions. The functions that are solutions do not change as a result of the sign choice, but the resulting eigenvalues and the arguments to the functions are different in the two regions. The following convention is introduced to make a distinction between the solutions and eigenvalues in the two regions:

$$\theta(x^+, y^+) = \begin{cases} \sum_{m=1}^{\infty} A_m \exp(\lambda_m x^+)\phi(\lambda_m, y^+); & x^+ < 0 \text{ (preflame)} \\ \sum_{m=1}^{\infty} B_m \exp(-\beta_m x^+)\psi(\beta_m, y^+); & x^+ > 0 \text{ (postflame)} \end{cases} \quad (21)$$

The series solutions preceding result from the fact that infinitely many eigenvalues satisfy the second boundary condition, and associated with each such eigenvalue is an eigenfunction Y_1, which is a solution to the ODE. Equation (21) automatically satisfies the boundary conditions at plus and minus infinity for x^+ and the boundary conditions in the y^+ direction. Therefore, the only remaining unknowns are the coefficients A_m and B_m. To evaluate them we must derive an orthogonality condition and invoke it to solve for the coefficients. This is accomplished in the next section.

Table 1 Definitions of parameters in Eq. (15)

	Preflame	Postflame
PI	$-\frac{1}{2} i \sqrt{\frac{3}{2}\alpha_n Pe}$	$-\frac{1}{2}\sqrt{\frac{3}{2}\alpha_n Pe}$
$a1$	$\frac{2i\alpha_n^{3/2}+\sqrt{6Pe}-3iPe\alpha_n^{1/2}}{4\sqrt{6Pe}}$	$-\frac{2\sqrt{6}\alpha_n^{3/2}-6\sqrt{Pe}+3Pe\sqrt{6\alpha_n}}{24\sqrt{Pe}}$
$b1$	$\frac{1}{2}$	$\frac{1}{2}$
$c1$	$i\sqrt{\frac{3Pe\alpha_n}{2}}y^{+2}$	$\sqrt{\frac{3Pe\alpha_n}{2}}y^{+2}$
$a2$	$-2a1$	$-2a1$
$b2$	$\sqrt[4]{-\frac{3}{2}Pe\alpha_n}y^+$	$\sqrt[4]{\frac{3}{2}Pe\alpha_n}y^+$

IV. Evaluation of Coefficients

Substituting Eq. (21) into the jump conditions (8a) and (8c) evaluated at the flame ($x^+ = 0$) leads to

$$\sum_{m=1}^{\infty} B_m \psi_m = \sum_{m=1}^{\infty} A_m \phi_m \quad (22)$$

$$\sum_{m=1}^{\infty} A_m \lambda_m \phi_m + \sum_{m=1}^{\infty} B_m \beta_m \psi_m = 1 \quad (23)$$

Our task is to find A_m and B_m using these two equations. Returning to the ODE (12) and writing it for two different eigenvalues gives

$$Y_m'' + (\alpha_m^2 \mp \alpha_m Pe U^+(y^+))Y_m = 0 \quad (24)$$

$$Y_n'' + (\alpha_n^2 \mp \alpha_n Pe U^+(y^+))Y_n = 0 \quad (25)$$

We find an orthogonality condition by computing the following integral:

$$\int_0^1 (\text{Eq. (24)} Y_n - \text{Eq. (25)} Y_m) \mathrm{d}y^+$$

This gives

$$\int_0^1 (Y_m'' Y_n - Y_n'' Y_m)\mathrm{d}y^+ + \int_0^1 (\alpha_m^2 - \alpha_n^2 \mp (\alpha_m - \alpha_n) Pe U^+(y^+))Y_m Y_n \mathrm{d}y^+ = 0 \quad (26)$$

The first term in Eq. (26) can be shown to be zero by integrating by parts and applying the boundary conditions applicable to the Y function. This leaves (after simplification) the following orthogonality condition that arises from the second term in Eq. (26):

$$\int_0^1 (\alpha_m + \alpha_n \mp Pe U^+(y^+))Y_m Y_n \mathrm{d}y^+ = 0; \qquad m \neq n \quad (27)$$

Equation (27) treats the orthogonality condition in a generic fashion (i.e., it does not distinguish between the eigenvalues and functions in the preflame and postflame regions). The minus or plus in Eq. (27) identifies the flow region, and the eigenvalues and eigenfunctions would be those corresponding to the particular flow region:

$$(\alpha = \lambda; Y = \phi) \quad \text{for } x^+ < 0 \qquad (\alpha = \beta; Y = \psi) \quad \text{for } x^+ > 0 \quad (28)$$

This orthogonality condition is different from a typical Sturm–Liouville orthogonality. This is because the ODE for the Y equation has the eigenvalues appearing in a nonlinear fashion and therefore does not follow the Sturm–Liouville pattern. The orthogonality condition in the preflame and postflame zones varies according to the minus or plus sign in the preceding equation. Now we can use the orthogonality condition (27) to obtain the coefficients A_m and B_m from the jump conditions. Reference [13] gives an elegant procedure for evaluating these coefficients for a heat transfer problem analogous to the one presented here. There are two important differences, however. The problem solved in the reference is analogous only to the postflame region (where the flow direction is away from the inlet) and requires the introduction of an artificial jump in the wall temperature. As we will see shortly, the nonlinear occurrence of the eigenvalues in the ODE for the Y equation requires the matching conditions to have a discontinuity or jump condition. In the heat transfer problem [13], this is introduced by means of a

sudden change in the wall temperature. In contrast, in our flame in a channel formulation, the jump condition occurs as a natural consequence of heat production at the flame. We start to derive the closed-form expression for the coefficients by performing the following manipulations to isolate A_n:

$$\int_0^1 \text{Eq. (22)} \times (-PeU^+(y^+) + \lambda_n)\phi_n \mathrm{d}y^+ \tag{29}$$

This leads to

$$\begin{aligned}\int_0^1 \sum_{m=1}^{\infty} B_m(-PeU^+(y^+) + \lambda_n)\phi_n\psi_m \mathrm{d}y^+ \\ = A_n \int_0^1 (-PeU^+(y^+) + \lambda_n)\phi_n^2 \mathrm{d}y^+ \\ + \sum_{\substack{m=1 \\ m\neq n}}^{\infty} \int_0^1 A_m(-PeU^+(y^+) + \lambda_n)\phi_n\phi_m \mathrm{d}y^+\end{aligned} \tag{30}$$

The second term on the right-hand side can easily be identified as being part of the orthogonality condition (for the preflame). Therefore, we can use Eq. (27) to rewrite Eq. (30) as follows:

$$\begin{aligned}\int_0^1 \sum_{m=1}^{\infty} B_m(-PeU^+(y^+) + \lambda_n)\phi_n\psi_m \mathrm{d}y^+ \\ = A_n \int_0^1 (-PeU^+(y^+) + \lambda_n)\phi_n^2 \mathrm{d}y^+ \\ + \int_0^1 \sum_{\substack{m=1 \\ m\neq n}}^{\infty} (-A_m\lambda_m\phi_n\phi_m)\mathrm{d}y^+\end{aligned} \tag{31}$$

Simplifying the sum on the right-hand side gives

$$\begin{aligned}\int_0^1 \sum_{m=1}^{\infty} B_m(-PeU^+(y^+) + \lambda_n)\phi_n\psi_m dy^+ \\ = A_n \int_0^1 (-PeU^+(y^+) + 2\lambda_n)\phi_n^2 \mathrm{d}y^+ \\ + \int_0^1 \sum_{m=1}^{\infty} (-A_m\lambda_m\phi_n\phi_m)\mathrm{d}y^+\end{aligned} \tag{32}$$

Now we use the second jump condition and do the following manipulation:

$$\int_0^1 \text{Eq. (23)} \times \phi_n \mathrm{d}y^+ \tag{33}$$

This gives

$$\int_0^1 \sum_{m=1}^{\infty} A_m\lambda_m\phi_m\phi_n \mathrm{d}y^+ = \int_0^1 \phi_n \mathrm{d}y^+ - \int_0^1 \sum_{m=1}^{\infty} B_m\beta_m\psi_m\phi_n \mathrm{d}y^+ \tag{34}$$

The fact that we have this naturally occurring jump condition in terms of the derivative of the temperature across the flame enables us to accommodate the nonlinearity of the eigenvalue in the ODE for Y. Inserting Eq. (34) into Eq. (32) and rearranging gives

$$\begin{aligned}A_n \int_0^1 (-PeU^+(y^+) + 2\lambda_n)\phi_n^2 \mathrm{d}y^+ = \int_0^1 \phi_n \mathrm{d}y^+ \\ + \sum_{m=1}^{\infty} B_m \int_0^1 (-PeU^+(y^+) + \lambda_n - \beta_m)\phi_n\psi_m \mathrm{d}y^+\end{aligned} \tag{35}$$

The term multiplying A_n on the left-hand side of Eq. (35) can be evaluated, as can the first term on the right-hand side. The second term on the right-hand side looks messy, as it couples the eigenfunctions and eigenvalues from the pre- and postflame regions in a complex fashion. However, if we consider the ODEs for the Y function in the pre- and postflame regions,

$$\phi_n'' + (\lambda_n^2 - \lambda_n PeU^+(y^+))\phi_n = 0 \tag{36}$$

$$\psi_m'' + (\beta_m^2 + \beta_m PeU^+(y^+))\psi_m = 0 \tag{37}$$

Following the same approach used to derive Eq. (27), we compute the following:

$$\int_0^1 (\text{Eq. (36)} \times \psi_m - \text{Eq. (37)} \times \phi_n)\mathrm{d}y^+ \tag{38}$$

This leads to

$$\begin{aligned}\int_0^1 (\phi_n''\psi_m - \phi_n\psi_m'')\mathrm{d}y^+ + (\lambda_n + \beta_m) \\ \times \int_0^1 (-PeU^+(y^+) + \lambda_n - \beta_m)\phi_n\psi_m \mathrm{d}y^+ = 0\end{aligned} \tag{39}$$

Again, because of the boundary conditions (13a) and (13b), the first integral (after integration by parts) can be easily shown to be zero (as both λ and β are positive numbers). This means that the second integral is also zero. Using this result in Eq. (35), we obtain

$$A_n = \frac{\int_0^1 \phi_n \mathrm{d}y^+}{\int_0^1 (-PeU^+(y^+) + 2\lambda_n)\phi_n^2 \mathrm{d}y^+} \tag{40}$$

Similarly, we can also show

$$B_n = \frac{\int_0^1 \psi_n \mathrm{d}y^+}{\int_0^1 (PeU^+(y^+) + 2\beta_n)\psi_n^2 \mathrm{d}y^+} \tag{41}$$

Therefore, separation of variables yields a closed-form analytical expression for the temperature field in the channel. The solution is given by Eq. (21) and the values of the coefficients are given by Eqs. (40) and (41).

V. Eigenvalues

The eigenvalues are obtained from Eq. (20), which is a generic representation of the eigenequation. It is clear, however, that the function Y itself changes based on the type of flow and the arguments to the function change based on the region of the flow (pre- or postflame). The eigenvalues can be computed analytically for plug flow, but must be computed numerically for Hagen–Poiseuille flow. We found by trial and error that including the first 30 terms (with eigenvalues and associated eigenfunctions) in the summation in Eq. (21) was sufficient to obtain an accuracy of about 1% in the analytical solution. This was established by comparing the values for the nondimensional temperature θ at the flame produced by the solutions in the pre- and postflame regions. Note that the difference between the nth and $(n + 1)$th eigenvalues approaches the value π for all values of the Péclet number for both types of flows. This is consistent with other heat transfer analyses of similar parallel-plate problems [13].

VI. Comparison with CFD

The predictions of the analytical model for Hagen–Poiseuille flow were validated via comparison with two-dimensional CFD simulations. A commercial CFD package, CFD-ACE+ [16], was used to solve the 2-D steady incompressible Navier–Stokes equations (43) and (44) [17] and the energy equation (42) [18] on a structured computational grid based on the geometry illustrated in Fig. 1:

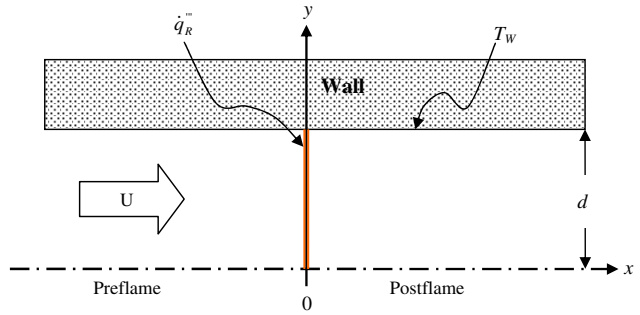

Fig. 1 Infinitely thin flame stabilized in a channel between two parallel plates.

$$\nabla \bullet (\rho \vec{V} h_0) = \nabla \bullet (k_{\text{eff}} \nabla T) + \left[\frac{\partial(u\tau_{xx})}{\partial x} + \frac{\partial(u\tau_{yx})}{\partial y}\right] + \left[\frac{\partial(v\tau_{xy})}{\partial x} + \frac{\partial(v\tau_{yy})}{\partial y}\right] \tag{42}$$

$$\nabla(\rho \vec{V} u) = -\frac{\partial P}{\partial x} + \left(\frac{\partial \tau_{xx}}{\partial x} + \frac{\partial \tau_{yx}}{\partial y}\right) \tag{43}$$

$$\nabla(\rho \vec{V} v) = -\frac{\partial P}{\partial y} + \left(\frac{\partial \tau_{xy}}{\partial x} + \frac{\partial \tau_{yy}}{\partial y}\right) \tag{44}$$

where k_{eff} is the thermal conductivity of the gas, T is the absolute temperature, u and v are the x-component and y-component velocities, ρ is the density, P is the static pressure, τ is the viscous stress, and $h0$ is the stagnation enthalpy, which is defined as

$$h_0 = i + \frac{p}{\rho} + \frac{1}{2}(u^2 + v^2) \tag{45}$$

where i is the internal energy. Equations (42–45) were solved subject to boundary and initial conditions equivalent to those applied to develop the analytical model.

The computational grid breaks into 3 domains, as illustrated in Fig. 2: a 100-mm-long preflame domain bounded by the inlet plane at the left, solid walls at the top and bottom, and a fluid interface at the right; a 0.1-mm-long flame domain bounded by fluid interfaces at the left and right and solid walls at the top and bottom; and a 100-mm-long postflame region with a fluid interface on the left, a fluid outlet on the right, and solid walls at the top and bottom. The structured grid is 5×200.1 mm and contains 24,745 cells. It is coarsest at the inlet and outlet and most refined in the center (where the flame is located) to ensure that streamwise temperature gradients are adequately resolved.

The minimum number of cells required to provide an accurate solution was determined by performing a grid convergence test for a high Péclet number case ($Pe = 10$) based on the maximum centerline flow velocity $U_{\max}$ and peak flame-zone temperature $T_{\max}$.

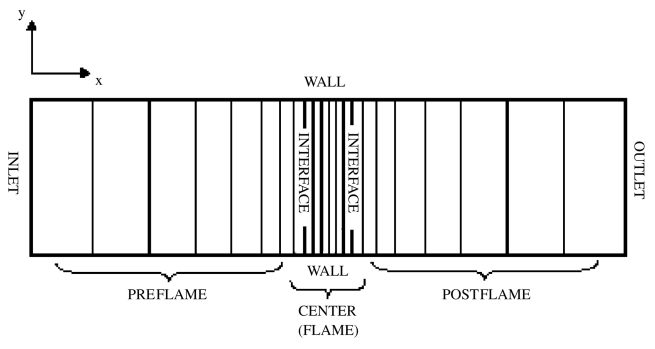

Fig. 2 Representative computational grid.

It was found that a grid of 17,400 cells allows for both $U_{\max}$ and $T_{\max}$ to change by less than 0.1% upon further grid refinement.

The boundary conditions at the inlet are 500 K gas temperature and a fully developed parabolic velocity profile ($u_{\text{mean}} = 0.02175$ m/s for $Pe = 1$ and $u_{\text{mean}} = 0.2175$ m/s for $Pe = 10$) for Hagen–Poiseuille flow. No slip is enforced at the walls. Heat transfer is allowed between the walls and the fluid, but the walls are assumed to be isothermal at 500 K. The pressure at the exit boundary is 1 atm. The flame is represented as a constant volumetric heat source of 8.5×10^7 W/m^3 located in the center domain. This value was identified by trial and error as the one that produced equal gas temperatures at the inlet and outlet of the center domain. This was necessary to ensure that the boundary conditions used to develop the analytical solution (i.e., that the pre- and postflame temperatures be equal at the flame) were properly represented. The fluid density, specific heat, and thermal conductivity of the gas were 0.706 kg/m^3, 1029 J/kg · K, and 0.0395 W/mK, respectively, in all of the simulations. All cells in the computational domain were initialized to the mean flow conditions at the inlet. The Péclet number was varied from 1 to 10 by changing the flow velocity.

Gradients were computed using a blended quasi-second-order spatial differencing scheme with 90% upwinding and 10% backward Euler. The pressure, velocity, and enthalpy were found using a conjugate-gradient-squared solver with preconditioning. A numerical simulation was considered to be converged when the L_2 norm of all residuals was reduced to at least 1.0×10^{-7}. Once a converged solution was obtained, the temperature distribution was exported to CFD-VIEW, from which the centerline and local temperature profiles were extracted. All simulations were performed using a Dell x86-based PC with dual 3391 MHz, Model 3 Stepping 4 Intel processors and 2 GB of RAM.

Figure 3 shows a typical temperature field computed using the analytical solution for the HP-flow situation. It shows, appropriately, that the gas temperature peaks at the flame location ($x^+ = 0$) and decreases as one moves upstream, downstream, or to the walls.

Figures 4 and 5 compare the analytical and CFD solutions. Figure 4 shows axial temperature profiles at 3 different vertical positions in the channel ($y^+ = 0$, 0.4, and 0.8) for 2 Péclet numbers ($Pe = 1$ and 5). These Péclet numbers were chosen because the flow velocities and dimensions generally associated with microcombustors and burners (our interest here) lead to Péclet numbers in the range of 1 to 10. In contrast, Péclet numbers associated with conventional scale devices are usually greater than 35. Figure 5 shows transverse temperature profiles at $Pe = 1$ and 5. The maximum difference between the analytical model and the numerical solution is less than 5% over the entire domain for both Péclet numbers, indicating that the analytical solution is valid. Interestingly, the peak gas temperature does not necessarily occur along the channel centerline, as shown in Figs. 5b and 6b. The reasons for this and the consequences for the Nusselt number will be discussed later.

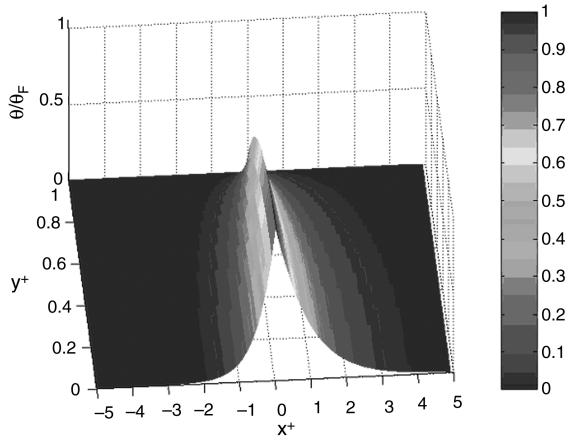

Fig. 3 Nondimensional 2-D temperature (θ/θ_F) field ($Pe = 1$).

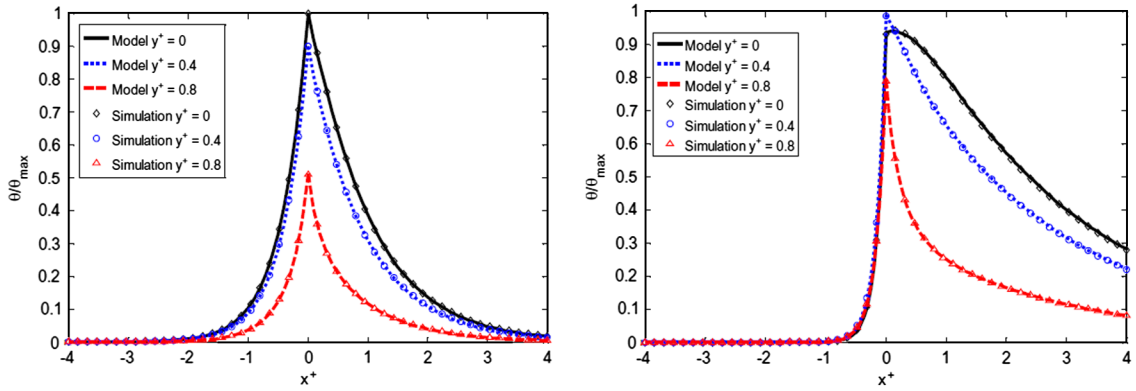

Fig. 4 Comparison of axial temperature profiles predicted by the analytical model and the CFD simulations for three transverse (y^+) locations with Hagen–Poiseuille flow: a) $Pe = 1$ and b) $Pe = 5$.

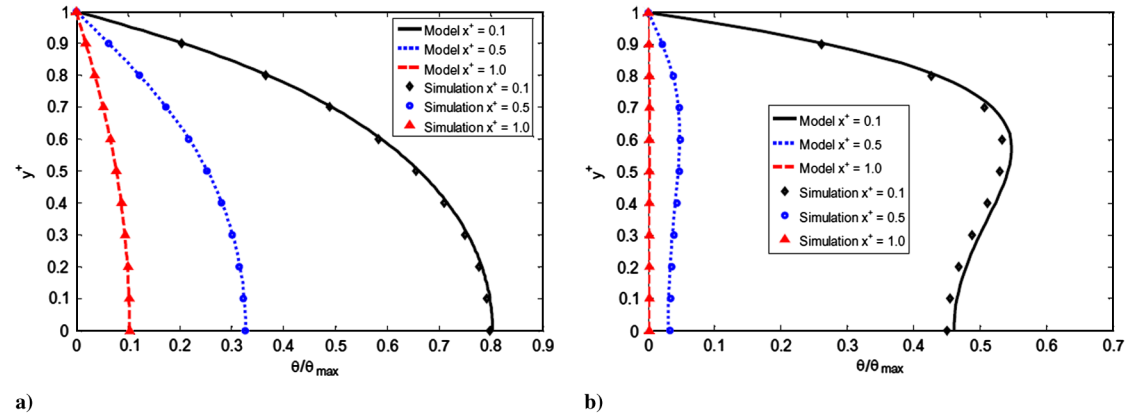

Fig. 5 Comparison of transverse temperature profiles predicted by the analytical model and the CFD simulations for three axial (x^+) locations for Hagen–Poiseuille flow: a) $Pe = 1$ and b) $Pe = 5$.

VII. Results and Discussion

A. Low Péclet Number

Figure 6 shows the ratio of the average temperature across the channel (in the transverse or y^+ direction) to the nondimensional flame temperature as a function of axial position in the channel when the Péclet number is relatively small.

The mean temperature profile is symmetric about the reaction zone and insensitive to flow velocity, velocity profile, or channel height at low Péclet numbers, because the convective transport term in Eq. (5) is small in comparison with the conduction terms.

B. Moderate Péclet Number

Figure 7 shows the ratio of the average temperature across the channel (in the transverse or y^+ direction) to the nondimensional flame temperature as a function of axial position in the channel for moderate values of the Péclet number. In both the plug-flow and Hagen–Poiseuille-flow cases, increasing the Péclet number causes the axial temperature distribution to become more asymmetric about the flame (heat release) zone. The asymmetry arises because the effect of the convective term is different in the pre- and postflame regions.

To see this, return to Eq. (5) and consider two positions both a distance δ from the flame but located in the pre- and postflame regions, respectively. In the postflame region, $\partial\theta/\partial x^+ < 0$ which means that the convective term acts with (i.e., in the same direction or tends to augment) the axial diffusive term ($\partial^2\theta/\partial x^{+2}$). This leads to a net increase in axial thermal transport and a temperature increase over the zero velocity case at the arbitrary location $x^+ = \delta$ in the postflame. In the preflame region, however, $\partial\theta/\partial x^+ > 0$ and the convective term acts against the axial diffusive term leading to a net temperature decrease at $x^+ = -\delta$. Increasing the Péclet number increases the level of distortion by increasing the difference between axial diffusive and convective processes in the pre- and postflame regions. This effect distorts axial temperature profiles in both the plug- and Hagen–Poiseuille-flow cases.

In the Poiseuille-flow case, however, the velocity profile causes the importance of the convective term relative to the axial diffusive term to decrease as one moves away from the channel centerline. In the postflame, this just reduces the augmentation of the axial thermal transport, and the maximum temperature still occurs at the channel center and decreases as one moves toward the wall. In the preflame, however, the convective term acts against the axial diffusive term. The reduction in the net thermal transport in the axial direction is greatest at the centerline and decreases as one moves toward the wall. This means that the peak in the transverse temperature profile does not occur at the channel center (as it does in the postflame), but at some intermediate point between the center and the wall, as shown in Fig. 6b. Increasing the Péclet number drives the peak temperature in the transverse direction farther from the channel centerline and closer to the walls. For $Pe > 30$, the flame is essentially a discontinuity, the problem is mostly one-dimensional, and a two-dimensional solution is not required.

C. Nusselt Number

The Nusselt number is defined as the ratio of the convective heat flux to the conductive heat flux. It is usually written in terms of a heat transfer coefficient h, the thermal conductivity of the gas k, and a characteristic length scale for heat transfer, which is taken to be the hydraulic diameter d_c in this case:

$$Nu = \frac{hd_c}{k} \tag{46}$$

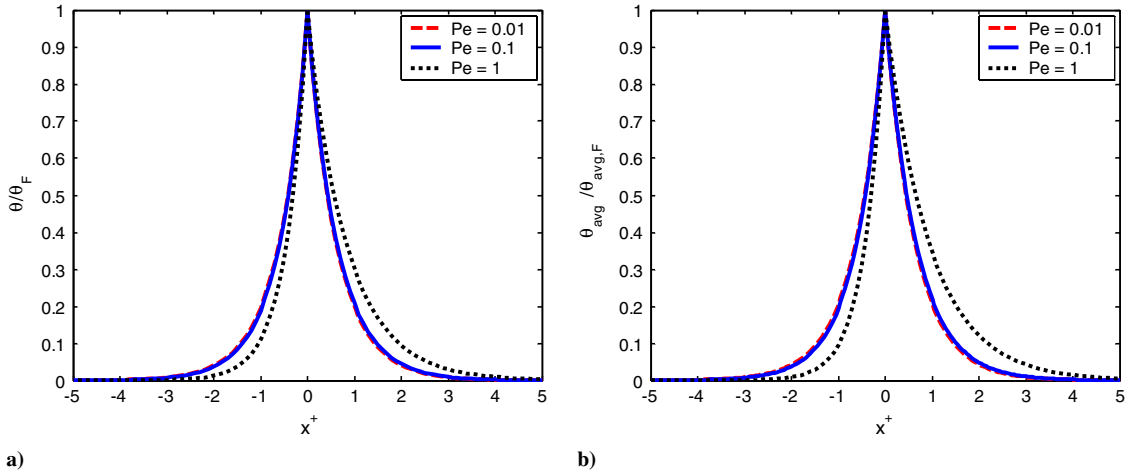

Fig. 6 Nondimensional temperature profile ($\theta_{\text{avg}}/\theta_{\text{avg},F}$) in the low Péclet limit: a) plug flow and b) Hagen–Poiseuille flow.

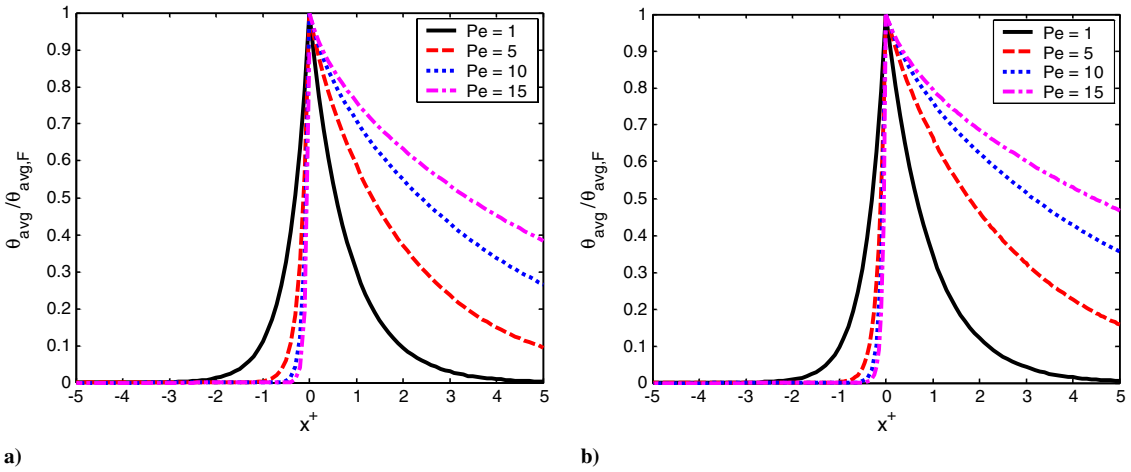

Fig. 7 Nondimensional temperature profile ($\theta_{\text{avg}}/\theta_{\text{avg},F}$) for plug and HP flows in the high Péclet limit.

The exact solution for the temperature profile can be used to compute an overall Nusselt number for the problem as well as to develop a correlation for the variation of Nusselt number with downstream distance. The latter is useful in one-dimensional numerical simulations of reacting flow with multistep-gas-phase chemistry [19], in which a computationally efficient method for incorporating two-dimensional heat transfer effects is required. The local heat transfer coefficient is given by

$$h_{x^+} = -\frac{k}{d}\frac{(\partial\theta/\partial y^+)|_{y^+=1}}{\theta_{\text{avg}}} \tag{47}$$

Inserting Eq. (47) into Eq. (46) and assuming a two-dimensional planar passage ($d_c = 4d$) gives

$$Nu_{x^+} = -4\frac{(\partial\theta/\partial y^+)|_{y^+=1}}{\theta_{\text{avg}}} \tag{48}$$

In this expression, θ_{avg} is the mean temperature of the flow:

$$\theta_{\text{avg}}(x^+) = \frac{\int_0^1 U(y^+)\theta(x^+, y^+)\mathrm{d}y^+}{\int_0^1 U(y^+)\mathrm{d}y^+} \tag{49}$$

Figure 8 shows the variation of Nusselt number with downstream distance for a range of Péclet numbers. In plug flow, the Nusselt number peaks at the flame and rapidly decreases to the value π^2 as x^+ goes to $\pm\infty$. This is consistent with other solutions for heat transfer between parallel plates at constant temperature [20]. In Hagen–Poiseuille flow, however, the situation is quite different. Although the solution also asymptotes to π^2 as x^+ goes to ∞, it asymptotes to different values (that depend on the Péclet number) as x^+ goes to $-\infty$. This curious behavior in the preflame is another consequence of the effect of the velocity profile on the competition between convection and axial conduction in the preflame region: Increasing the Péclet number moves the peak in the transverse temperature profile closer to the wall. This increases the Nusselt number by increasing the temperature gradient at the wall. The Nusselt number approaches a constant far upstream, because the temperature gradient at the wall goes to zero at the same rate as the mean temperature.

Figure 9 shows that although the Nusselt number in the postflame is a constant that is independent of Péclet number, it is not a constant in the preflame when the Péclet number is of order 1 or greater. This is important, because currently accepted practice in the simulation of reacting flows in microcombustors is to choose a single Nusselt number to represent gas–wall heat transfer over the entire computational domain. Given that preheating of the mixture by the structure in the preflame region is a critical aspect of microcombustor performance [4,21,22] and that the potential variation in preflame Nusselt number is large (up to 3 orders of magnitude), it is clear that incorporating this effect will be important in future simulations. Table 2 gives the asymptote values of the pre- and postflame Nusselt numbers for different values of Péclet for HP flow. These values may be used in future simulations that model constant-wall-temperature combustors after estimating the Péclet number for the application. The values in the table show that the Nusselt number increases rapidly in the preflame region beyond a Péclet number of 1. This makes sense, because the flow becomes essentially one-dimensional at $Pe > 30$.

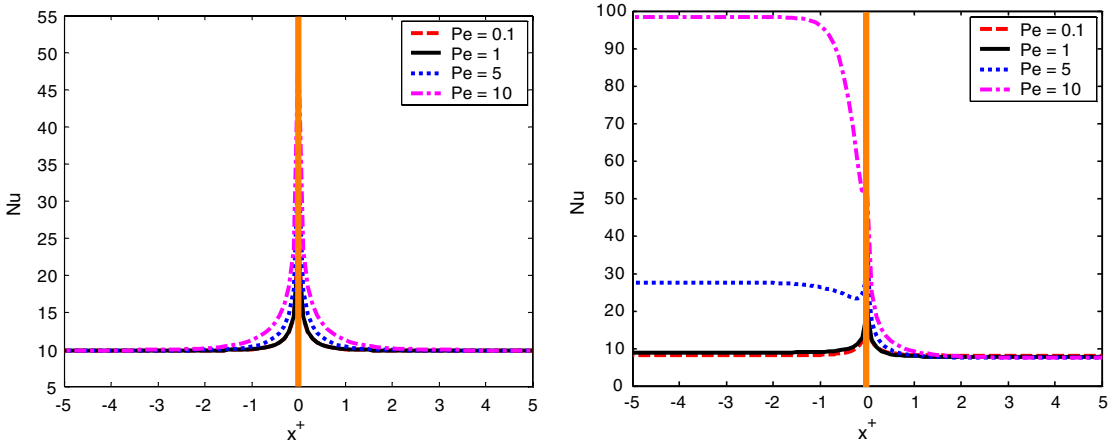

Fig. 8 Nusselt number vs axial distance for different Péclet numbers: a) plug flow and b) Poiseuille flow.

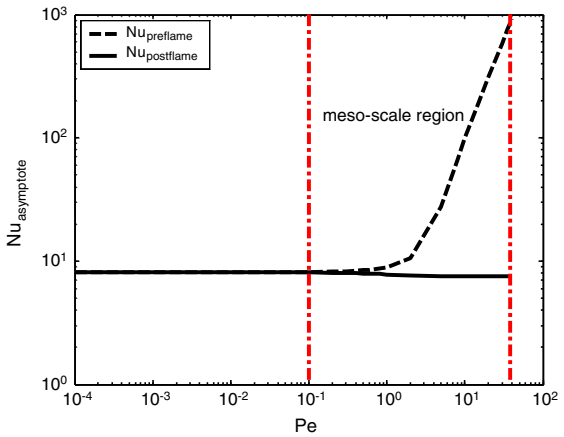

Fig. 9 Nusselt asymptote as a function of Péclet for H-P flow.

Table 2 Nusselt number asymptote values for pre- and postflame regions for different Péclet numbers for H-P flow

Pe	Nu_{pre}	Nu_{post}
0.0001	8.11747	8.11737
0.001	8.11793	8.11692
0.01	8.12246	8.11244
0.02	8.12753	8.10749
0.05	8.14304	8.09293
0.1	8.16984	8.06952
0.2	8.22711	8.02579
0.3	8.28961	7.98592
0.4	8.35772	7.94958
0.5	8.43182	7.9165
0.6	8.51232	7.8864
0.8	8.6942	7.83411
1	8.90686	7.79088
2	10.5733	7.6629
5	27.6355	7.56931
8	66.4142	7.55258
10	98.3997	7.54842
15	193.776	7.54418
20	308.596	7.54267
25	440.381	7.54196
30	587.348	7.54158
35	748.169	7.54135
40	921.823	7.5412

VIII. Conclusions

A simple extension to the classical Graetz problem has been used to develop an analytical solution for the temperature field in a planar channel with localized heat release due to combustion. The solution has been validated via comparison with CFD and shows that the Péclet number is the principal parameter affecting the temperature distribution in the channel. The solution may also be used to obtain analytical expressions for the Nusselt number. Because the Péclet numbers associated with most microcombustors are in the intermediate regime ($1 < Pe < 10$), in which both conductive and convective (or transverse and axial) heat transfer modes are important, the results indicate that two-dimensional (or even three-dimensional) heat transfer models are required to properly model reacting flows in microcombustors.

Acknowledgments

The authors would like to thank the U.S. Air Force Office of Scientific Research (AFOSR) and Mitat Birkan, who supported this work under AFOSR F496200110435.

References

[1] Mehra, A., Zhang, X., Ayon, A. A., Waitz, I. A., Schmidt, M. A., and Spadaccini, C. M., "A Six-Wafer Combustion System for a Silicon Micro Gas Turbine Engine," *Journal of Microelectromechanical Systems*, Vol. 9, No. 4, 2000, pp. 517–527. doi:10.1109/84.896774

[2] Ronney, P. D., "Analysis of Nonadiabatic Heat-Recirculating Combustor," *Combustion and Flame*, Vol. 135, No. 4, 2003, pp. 421–439. doi:10.1016/j.combustflame.2003.07.003

[3] Daou, J., and Matalon, M., "Influence of Conductive Heat-Losses on the Propagation of Premixed Flames in Channels," *Combustion and Flame*, Vol. 128, No. 4, 2002, pp. 321–329. doi:10.1016/S0010-2180(01)00362-5

[4] Leach, T. T., and Cadou, C. P., "The Role of Structural Heat Exchange and Heat Loss in the Design of Efficient Silicon Micro-Combustors," *Proceedings of the Combustion Institute*, Vol. 30, No. 2, 2005, pp. 2437–2444. doi:10.1016/j.proci.2004.08.229

[5] Xu, B., and Ju, Y., "Theoretical and Experimental Studies on Mesoscale Flame Propagation and Extinction," *Proceedings of the Combustion Institute*, Vol. 30, No. 2, 2005, pp. 2445–2454.

[6] Kotani, Y., and Takeno, T., "Ignition and Combustion of Magnesium-Aluminum Alloy Particle Clouds in a Hot Gas Stream," *Proceedings of the Combustion Institute*, Vol. 19, No. 1, 1982, pp. 741–748.

[7] Takeno, T., and Sato, K., "An Excess Enthalpy Flame Theory," *Combustion Science and Technology*, Vol. 20, No. 1, 1979, pp. 73–84. doi:10.1080/00102207908946898

[8] Hase, K., Sato, K., and Takeno, T., "A Theoretical Study of Excess Enthalpy Flame," *Proceedings of the Combustion Institute*, Vol. 18, 1980, pp. 465–472.

[9] Cui, C., Matalon, M., Daou, J., and Dold, J., "Effects of Differential Diffusion on Thin and Thick Flames Propagating in Channels," *Combustion Theory and Modeling*, Vol. 8, No. 1, 2004, pp. 41–64. doi:10.1088/1364-7830/8/1/003

[10] Daou, J., and Matalon, M., "Influence of Conductive Heat-Losses on the Propagation of Premixed Flames in Channels," *Combustion and Flame*, Vol. 128, No. 4, 2002, pp. 321–339. doi:10.1016/S0010-2180(01)00362-5

[11] Graetz, L., "Über die Wärmeleitus der Fähigkeit von Flüssigkeiten," *Annalen der Physik und Chemie*, Vol. 18, 1883, pp. 79–94.

[12] Yin, X., and Bau, H., "The Conjugate Graetz Problem with Axial Conduction," *Journal of Heat Transfer*, Vol. 118, No. 2, 1996, pp. 482–484. doi:10.1115/1.2825871

[13] Lahjomri, J., and Oubarra, A., "Analytical Solution of the Graetz Problem with Axial Conduction," *Journal of Heat Transfer*, Vol. 121, No. 4, 1999, pp. 1078–1083. doi:10.1115/1.2826060

[14] Ebadian, M., and Zhang, H., "An Exact Solution of Extended Graetz Problem with Axial Heat Conduction," *International Journal of Heat and Mass Transfer*, Vol. 32, No. 9, 1989, pp. 1709–1717. doi:10.1016/0017-9310(89)90053-7

[15] Michelsen, M., and Villadsen, J., "The Graetz Problem with Axial Heat Conduction," *International Journal of Heat and Mass Transfer*, Vol. 17, No. 11, 1974, pp. 1391–1402.

[16] CFD-ACE+, Software Package, Ver. 2004, ESI US R&D, Inc., Santa Clara, CA, May 2004.

[17] Schlichting, H., *Boundary-Layer Theory*, 7th ed., McGraw–Hill, New York, 1979, pp. 47–69.

[18] Kays, W., and Crawford, M., *Convective Heat and Mass Transfer*, 2nd ed., McGraw–Hill, New York, pp. 26–29.

[19] Leach, T. T., Cadou, C. P., and Jackson, G. S., "Effect of Structural Conduction and Heat Loss on Combustion in Microchannels," *Combustion Theory and Modeling*, Vol. 10, No. 1, 2006, pp. 85–103. doi:10.1080/13647830500277332

[20] Kakac, S., and Yener, Y., *Convective Heat Transfer*, 2nd ed., CRC Press, Boca Raton, FL, 1995, pp. 132–180.

[21] Veeraragavan, A., and Cadou, C., "Experimental Burning Velocity Characteristics for Premixed Methane-Air Flames in a Simulated Microcombustor," 5th U.S. Combustion Meeting, Western States Section, Combustion Inst., Paper H06, Mar 2007.

[22] Heatwole, S., Veeraragavan, A., Buckley, S., and Cadou, C., "In-Situ Species and Temperature Measurements in a Millimeter-Scale Combustor," *Microscale Thermophysical Engineering*, Vol. 13, No. 1, 2009, pp. 54–76. doi:10.1080/15567260802662455

A. Prasad
Associate Editor